PAPER

Check for updates

Observation of Haldane magnetism in organically templated vanadium phosphate (enH$_2$)$_{0.5}$VPO$_4$OH†

A. Sh. Samarin,[a] S. S. Fedotov,[a] H.-J. Koo,[b] M.-H. Whangbo,[b,c] A. A. Gippius,[d,e] S. V. Zhurenko,[e] A. V. Tkachev,[e] L. V. Shvanskaya [ID] *[d,f] and A. N. Vasiliev [ID] *[d,f]

We prepared an organically templated magnet, (enH$_2$)$_{0.5}$VPO$_4$OH (enH$_2$ = diprotonated ethylenediamine), hydrothermally and characterized its crystal structure by powder X-ray diffraction and Fourier-transform infrared spectroscopy, and its physical properties by magnetization, specific heat and nuclear magnetic resonance measurements and density functional theory calculations. (enH$_2$)$_{0.5}$VPO$_4$OH consists of uniform chains of V^{3+} (d^2, S = 1) ions and exhibits Haldane magnetism with spin gap Δ = 59.3 K from the magnetic susceptibility $\chi(T)$ at $\mu_0 H$ = 0.1 T, which is reduced to 48.4 K at $\mu_0 H$ = 9 T according to the ^{31}P shift. The NMR data evidence the formation of a spin-glass state of unpaired S = 1/2 spins at $T_{S-G} \approx$ 3 K and indicate that the Haldane S = 1 spin chain segments are much longer in the organically templated magnet (enH$_2$)$_{0.5}$VPO$_4$OH than in the ammonium counterpart NH$_4$VPO$_4$OH. The single-ion anisotropy D and the interchain exchange J' in (enH$_2$)$_{0.5}$VPO$_4$OH and NH$_4$VPO$_4$OH were estimated in density functional calculations to find them very weak compared to the intrachain exchange J.

Introduction

Haldane's prediction[1] of a singlet ground state in quasi-one-dimensional integer-spin antiferromagnets with low single-ion anisotropy D has stimulated an intensive search for compounds satisfying the strict criteria for its existence based on the D/J and J'/J ratios, where J' and J are the interchain and the intrachain exchange interactions, respectively.[2] In chain compounds of S = 1 ions, the Haldane phase competes with the long-range ordered, dimerized and large-D phases. So far, ten metal–organic and three inorganic magnets based on Ni^{2+} (d^8, S = 1) (*i.e.*, Y$_2$BaNiO$_5$, SrNi$_2$V$_2$O$_8$ and PbNi$_2$V$_2$O$_8$) have been found to be Haldane magnets and hence have a spin gap between the continuum of excited states and the ground state.[3,4] Three more inorganic compounds, Ba$_2$V(VO$_4$)$_2$OH, AgVP$_2$S$_6$ and NH$_4$VPO$_4$OH, based on V^{3+} (d^2, S = 1) ions are also found to be Haldane magnets.[4,5] Here, we report synthesis and characterization of the first organically templated Haldane magnet based on V^{3+} ions, (enH$_2$)$_{0.5}$VPO$_4$OH, where enH$_2$ refers to the diprotonated ethylenediamine, H$_3$NCH$_2$CH$_2$NH$_3$$^{2+}$. On the basis of density functional calculations, we establish the location of (enH$_2$)$_{0.5}$VPO$_4$OH on the D/J *vs.* J'/J phase diagram.

Synthesis and X-ray diffraction

(enH$_2$)$_{0.5}$VPO$_4$OH was synthesized hydrothermally in one step by mixing 0.0008 mol of V$_2$O$_3$, 0.0016 mol of H$_3$PO$_4$ and 0.005 mol of H$_2$N(CH$_2$)$_2$NH$_2$ in 0.44 mol of deionized H$_2$O at 100 rpm stirring at room temperature in a 30 ml Teflon vessel. The information on chemicals used for the synthesis is given in Table S1 of ESI.† The vessel then was sealed in steel autoclave and the mixture was hydrothermally treated at 205 °C for 7 days under constant stirring (750 rpm). After that, the autoclave was naturally cooled down to room temperature, to obtain a pale-sandy fine powder sample. The latter was carefully filtrated and washed with deionized water 5 times by centrifugation. Then it was dried overnight at 75 °C in a vacuum oven and kept under inert (Ar) atmosphere until further use.

Powder X-ray diffraction (PXRD) patterns were collected with a Bruker D8 ADVANCE powder diffractometer ($\lambda_{CuK\alpha1}$ = 1.54051 Å, $\lambda_{CuK\alpha2}$ = 1.54433 Å) equipped with an energy dispersive detector LYNXEYE XE in Bragg–Brentano reflection geometry (5–130° 2θ, 0.02° scan step). The crystal structure was refined from the PXRD data with the TOPAS-Academic software package using the Rietveld method.[6] Isostructural (enH$_2$)$_{0.5}$FePO$_4$OH was used as a starting structural model.[7]

[a] Skolkovo Institute of Science and Technology, Moscow 121205, Russia

[b] Kyung Hee University, Seoul 02447, Republic of Korea

[c] North Carolina State University, Raleigh, North Carolina 27695-8204, USA

[d] Lomonosov Moscow State University, Moscow 119991, Russia.
E-mail: anvas2000@yahoo.com, lshvanskaya@mail.ru

[e] Lebedev Physical Institute, RAS, Moscow 119991, Russia

[f] National University of Science and Technology MISIS, Moscow 119049, Russia

†Electronic supplementary information (ESI) available. See DOI: https://doi.org/10.1039/d4dt01675k

The background was estimated by a set of polynomials, the calculation of the unit cell parameters and the refinement of the atomic coordinates were performed. According to the phase analysis no traceable impurities were observed, as shown in Fig. 1. Broad peak at about 70° is due to the sample holder. The inset to Fig. 1 represents the scanning electron microscopy (SEM) image of the sample showing its needle-like morphology. The calculated unit cell parameters are given in Table 1. Atomic fractional coordinates for $(en\text{H}_2)_{0.5}\text{VPO}_4\text{OH}$ according to the Rietveld refinement are given in Table S2 of ESI.†

As shown in Fig. 2a, $(en\text{H}_2)_{0.5}\text{VPO}_4\text{OH}$ possesses a layered structure, in which the VPO_4OH^- layers alternate with ribbons of $en\text{H}_2^{2+}$ cations running along the a axis. In each VPO_4OH^- layer, the chains of edge-sharing VO_5OH octahedra are interconnected by PO_4 groups (Fig. 2b). $(en\text{H}_2)_{0.5}\text{VPO}_4\text{OH}$ belongs to the structural type of $(en\text{H}_2)_{0.5}\text{MPO}_4\text{OH}$ (M = Fe, Ga)[7,8] and closely related to $\text{NH}_4\text{MPO}_4\text{OH}$ (M = V, Ga)[5,9] (see ESI and Fig. S1†).

Fourier-transform infrared spectroscopy

The presence of the ethylenediamine and hydroxyl groups in $(en\text{H}_2)_{0.5}\text{VPO}_4\text{OH}$ was confirmed by infrared spectroscopy, as shown in Fig. 3. Fourier-transform infrared (FTIR) spectra were
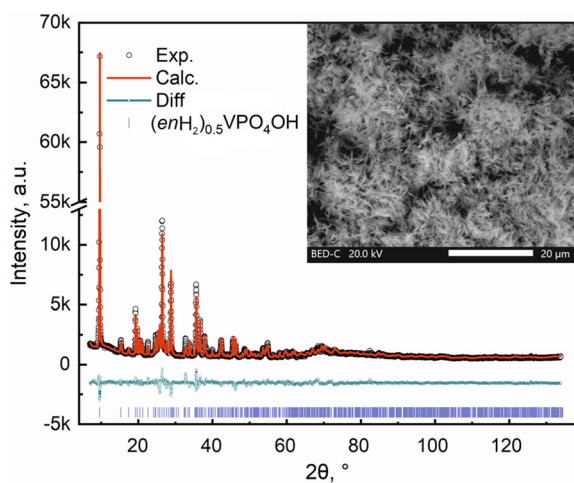

Fig. 2 (a) A perspective view of the crystal structure of $(en\text{H}_2)_{0.5}\text{VPO}_4\text{OH}$ showing that the VPO_4OH layers are separated by the layers of the $en\text{H}_2^{2+}$ cations. (b) A single VPO_4OH layer showing how the edge-sharing ribbon chains are interconnected by the PO_4 groups to form a VPO_4OH layer. Colors: vanadium atoms – light green, phosphorus atoms – yellow, oxygen atoms – red, nitrogen atoms – light blue, carbon atoms – intense blue, hydrogen atoms – pale pink.
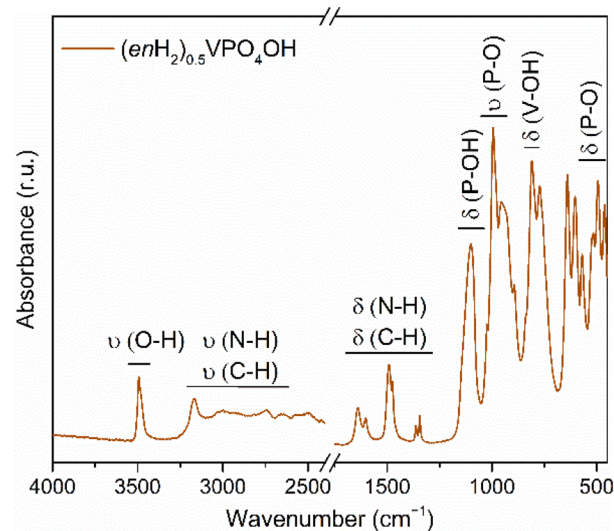

Fig. 1 Experimental, calculated and difference diffraction profiles of $(en\text{H}_2)_{0.5}\text{VPO}_4\text{OH}$. Inset: The SEM image of the sample.

Fig. 3 FTIR spectrum of $(en\text{H}_2)_{0.5}\text{VPO}_4\text{OH}$.

Table 1 Rietveld refinement of cell parameters of $(en\text{H}_2)_{0.5}\text{VPO}_4\text{OH}$

Formula	$(en\text{H}_2)_{0.5}\text{VPO}_4\text{OH}$
S.G.	$P2_1/c$
a, Å	4.5282(6)
b, Å	6.1098(12)
c, Å	18.5879(17)
β, °	94.781(3)
V, Å³	512.48(13)
Z	4
GOF	2.43
R_{exp}, %	3.17
R_p, R_{wp}, %	5.62, 7.73

collected with an ALPHA II compact FTIR spectrometer (Bruker). The spectra were recorded in the 4000–400 cm^{-1} range with 2 cm^{-1} resolution. The reproducibility was checked by probing three different spots of the same powder sample. The presence of the hydroxyl group is manifested by a sharp maximum located at 3492 cm^{-1} ($\nu(\text{OH})$).[10] The group between 3300 and 2400 cm^{-1} corresponds to the N–H and C–H vibrations in the $en\text{H}_2^{2+}$ moiety. The most intense maximum (~3166 cm^{-1}) is associated with N–H (stretch), which is involved in hydrogen bonding. At lower wavenumbers (1750–1250 cm^{-1}), three groups of peaks are observed, which reflect presence of $en\text{H}_2^{2+}$ in the interlayer space. The complex shape of the spectra in this range is defined by a joint C–H and N–H vibrations.[11] Taking into account few previous

reports about ethylenediamine-containing metal–organic compounds, we can assume that the first and second couples of maxima fall into the range of bending N–H modes and may also contain some contribution of C–H vibrations (most likely bending ones). The third couple of peaks corresponds to the C–H (bending and/or twisting) modes.[12–14] The maxima located in the 1100–500 cm^{-1} range (except the one at 810 cm^{-1} – δ(V–OH)) are related to the bending and stretching vibrations of the O–P–O bonds. The peak at 1100 cm^{-1} corresponds to the δ(P–OH).[9]

Thermodynamics

Thermodynamic properties of $(en\text{H}_2)_{0.5}\text{VPO}_4\text{OH}$, *i.e.*, the magnetization M and the specific heat C_P were measured using relevant options of "Quantum Design" Physical Properties Measurements System PPMS-9T in the temperature range 2–300 K in a magnetic field $\mu_0 H$ up to 9 T. The temperature dependence of the magnetic susceptibility, $\chi = M/H$, taken at $\mu_0 H = 0.1$ T in the field-cooled mode is shown in Fig. 4a. It shows a broad correlation hump centred at about 150 K, which is followed by a rapid increase on lowering the temperature. This upturn at low temperatures can be ascribed to a trace amount, n_imp, of impurities in the chain, which produce dangling bonds of spin $S = 1/2$ at the ends of the spin-chain segments.

The $\chi(T)$ curve can be fitted by the sum of Curie law

$$\chi = \chi_0 + C/(T - \Theta) \tag{1}$$

responsible for the impurities, and the susceptibility of the defect-free chain as given by the Padé expansion[15]

$$\chi_\text{chain} = \frac{N_\text{A}\mu_\text{B}^2 g^2 S(S+1)}{3k_\text{B}T} \times \exp\left(-\frac{\Delta}{k_\text{B}T}\right)$$

$$\times \frac{1 + \sum_{i=1}^{m} A_i\left(\frac{J}{k_\text{B}T}\right)^i}{1 + \sum_{j=1}^{n} B_j\left(\frac{J}{k_\text{B}T}\right)^j}. \tag{2}$$

where N_A, μ_B and k_B are the Avogadro number, Bohr magneton and Boltzmann constant, respectively. Under the assumption
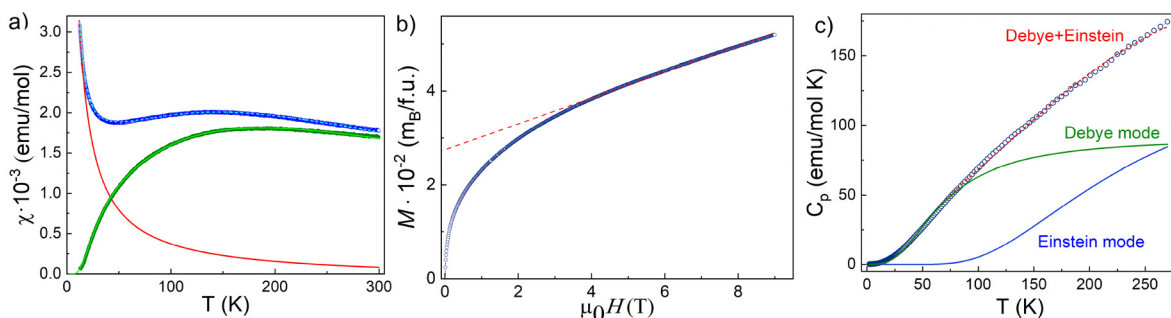
of $\Delta = 0.41J$ and g-factor $g = 2$, the best fit shown in Fig. 4a was obtained using the temperature-independent term $\chi_0 = -6.88 \times 10^{-5}$ emu mol^{-1}, the Curie constant $C = 0.045$ emu K mol^{-1}, the Weiss temperature $\Theta = -2.1$ K and the intrachain exchange parameter $J = 144.7$ K (hence, $\Delta = 59.3$ K). The value of C corresponds to $n_\text{imp} = 0.75\%$. Each impurity brings two $S = 1/2$ dangling spins at the ends of the Haldane chain segments. The value of χ_0 is in agreement with the sum of the Pascal constants of the individual ions in $(en\text{H}_2)_{0.5}\text{VPO}_4\text{OH}$, which equals to -7.72×10^{-5} emu mol^{-1}.[16] The negative sign of the Weiss temperature points to the weak antiferromagnetic coupling between the dangling bonds of spin $S = 1/2$.

The field dependence of magnetization in $(en\text{H}_2)_{0.5}\text{VPO}_4\text{OH}$ taken at 2 K is shown in Fig. 4b. The tangent to this curve shown by the dash line extrapolates to $2.7 \times 10^{-2} \mu_\text{B}$ per f.u., which corresponds to 1.35% of impurities. This estimation, which is higher than estimation obtained from the Curie–Weiss fitting reflects the field-induced polarization of spin $S = 1/2$ at the ends of the spin-chain segments forming the spin-glass state (see NMR section).

The temperature dependence of the specific heat in $(en\text{H}_2)_{0.5}\text{VPO}_4\text{OH}$ is shown in Fig. 4c. No anomalies were observed down to 2 K, which excludes the transition into a long-range ordered state. At room temperature, the value of C_P is still far from the Dulong-Petit limit $3RN = 374$ J mol^{-1} K, where the number of atoms per formula unit $N = 15$ and the universal gas constant $R = 8.314$ J mol^{-1} K. The experimental data can be fitted by the sum of Debye (temperature $\Theta_\text{D} = 282.5$ K and weight $a_\text{D} = 3.66$) and Einstein (temperature $\Theta_\text{E} = 734.5$ K and weight $a_\text{E} = 6.07$) modes, as shown by green and blue solid lines in Fig. 4c. These two modes reflect the presence of heavy (V, P) and light (H, C, N, O) atoms in the structure of $(en\text{H}_2)_{0.5}\text{VPO}_4\text{OH}$.

Nuclear magnetic resonance

NMR spectra of ^{31}P nuclei as well as their spin–lattice relaxation were measured using a custom designed phase coherent pulsed NMR spectrometer with direct quadrature signal detection at the carrier frequency at a constant magnetic field of 9 T

Fig. 4 (a) Temperature dependence of the magnetic susceptibility measured for $(en\text{H}_2)_{0.5}\text{VPO}_4\text{OH}$ using the field-cooled protocol at $\mu_0 H = 0.1$ T. The experimental data (blue symbols) are fitted by the sum of the impurity contribution (red solid line) and the defect-free chain contribution (green solid line). The latter was obtained by removing the impurity contribution. (b) Field dependence of the magnetization at 2 K. The red dash line is the tangent at high field. (c) Temperature dependence of specific heat (symbols) fitted by the sum of Debye (green line) and Einstein (blue line) modes.

in the temperature range of 2.5–310 K. For spectra accumulation, we used the Hahn spin echo pulse sequence augmented by the fast Fourier-transform summation method.[17–19] The nuclear spin–lattice relaxation rate was measured by means of the saturation recovery method.

The set of ^{31}P NMR spectra of $(enH_2)_{0.5}VPO_4OH$ is shown in Fig. S2 of the ESI† with four selected spectra measured at 4.5, 9, 150 and 310 K presented in the upper inset of Fig. 5. Similar to NH_4VPO_4OH,[5] the spectra consist of a single and almost symmetric line, which progressively broadens with decreasing temperature. The temperature dependence of the ^{31}P NMR linewidth estimated as a full width at half maximum (FWHM) is shown in the lower inset to Fig. 5. It is well described by the power law $\sim T^n$ with $n = -0.40 \pm 0.01$ in the entire temperature range investigated in contrast to NH_4VPO_4OH. Below 20 K, the latter shows the Curie–Weiss-like FWHM behavior, which was observed due to the magnetic contribution from the unpaired edge spins $S = 1/2$.[5]

The temperature dependence of the shift $K(T)$ taken as a position of the line maximum in relation to the Larmor frequency at $\mu_0H = 9$ T in 85% phosphoric acid aqueous solution is shown in Fig. 5, which exhibits a broad maximum at around 140 K similar to that observed in the $\chi(T)$ curve obtained at $\mu_0H = 0.1$ T at around 150 K. In the entire temperature range, the temperature dependence of the experimental $K(T)$ was successfully approximated by the Padé equation for Haldane chains (eqn (2)) with $J = 118(2)$ K providing the gap value $\Delta = 48.4$ K. This gap is smaller than that obtained from the $\chi(T)$ curve since it was obtained at a much higher field (i.e., 9 T). Note, the determination of the gap from the ^{31}P shift is independent from the impurity contribution. In contrast to NH_4VPO_4OH,[5] $(enH_2)_{0.5}VPO_4OH$ does not show a pronounced low temperature Curie–Weiss-like behavior of the ^{31}P shift, which originates from unpaired $S = 1/2$ spins at the edges of

finite length Haldane $S = 1$ spin chains. This observation is in line with the magnetic susceptibility data, which show that $(enH_2)_{0.5}VPO_4OH$ has much less paramagnetic centers than does NH_4VPO_4OH (i.e., 0.75% vs. 3% (ref. 5)), indicating that the Haldane $S = 1$ spin chain segments of $(enH_2)_{0.5}VPO_4OH$ are much longer than those of NH_4VPO_4OH.

The ^{31}P nuclear magnetization recovery curves exhibit a double exponential behavior with the fast and slow components approximated by a simple and a stretched exponential function, $\exp[-(\tau/T_{1fast})]$ and $\exp[-(\tau/T_{1slow})^\beta]$ ($0 \leq \beta \leq 1$), respectively. The fast component is dominated (one order of magnitude) above 40 K and is therefore attributed to the relaxation channel via the $S = 1$ electronic spins of the Haldane chains. Apparently, the slow relaxation term is caused by unpaired edge $S = 1/2$ spins. Below 30 K, the Haldane chain approaches its spin singlet ground state and the relative weights of two relaxation components become almost equal. With decreasing temperature below 10 K, both $1/T_{1fast}$ and $1/T_{1slow}$ start to increase reaching a maximum at around 3 K. Such a behavior is characteristic for the formation of a disordered spin-glass of unpaired $S = 1/2$ spins at $T_{S–G} \approx 3$ K. The latter originates from a critical slowing down of the spin fluctuations when approaching the freezing temperature,[20,21] as observed in NH_4VPO_4OH[5] as well. Temperature dependences of the fast and slow ^{31}P spin–lattice relaxation rates in $(enH_2)_{0.5}VPO_4OH$ measured at 9 T are shown in Fig. S3 of ESI.†

Density functional analysis

We now determine the intrachain spin exchange J, the interchain spin exchange J' and the single-ion anisotropy D of $(enH_2)_{0.5}VPO_4OH$ based on density functional theory (DFT) calculations, to establish its position on the Sakai–Takahashi phase diagram[2] described in terms of the D/J and $2J'/J$ ratios. The parameters J and J' are obtained by the energy-mapping analysis[22–24] based on DFT calculations.[25–27] Since $(enH_2)_{0.5}VPO_4OH$ is a magnetic insulator, our energy-mapping analysis was carried in DFT+U calculations[28] (with $U_{eff} = 2$ and 3 eV on V) using the spin Hamiltonian

$$H_{spin} = \sum_{i>j} J_{ij}\vec{S}_i \cdot \vec{S}_j, \qquad (3)$$

where $J_{ij} = J$ or J', so that antiferromagnetic (ferromagnetic) spin exchanges were represented by positive (negative) J_{ij} values, while the parameter D was calculated by DFT+U+SOC calculations[29] (see the ESI† for details). With $U_{eff} = 2$ eV, the calculated J value is quite close to the experimental one, namely, 146.8 K for $(enH_2)_{0.5}VPO_4OH$. For NH_4VPO_4OH, the best agreement, namely 92.8 K, with experimental data[5] is achieved also at $U_{eff} = 2$ eV. Relative energies of the ordered spin states obtained from DFT+U calculations are given in Table S3 of ESI,† while the relative energies ΔE of the $\|z$ and $\perp z$ spin orientations of $(enH_2)_{0.5}VPO_4OH$ and NH_4VPO_4OH obtained from DFT+U+SOC calculations as well as the spin and orbital moments μ_S and μ_L are given in Table S4.† The calculated J, J' and D values for $(enH_2)_{0.5}VPO_4OH$ are summarized
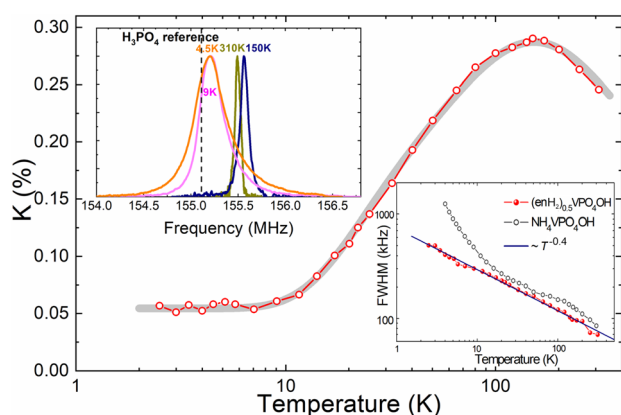
Fig. 5 Temperature dependence of the ^{31}P NMR shift measured for $(enH_2)_{0.5}VPO_4OH$. The thick gray line is the best fit to eqn (2). The upper inset: ^{31}P NMR spectra taken at 4.5, 9, 150 and 310 K. The position of the Larmor frequency in 85% H_3PO_4 aqueous solution at $\mu_0H = 9$ T is indicated by the dashed line. The lower inset: The FWHM of ^{31}P NMR spectra as a function of temperature in $(enH_2)_{0.5}VPO_4OH$ and NH_4VPO_4OH (adopted from ref. 5).

in Table 2, where the corresponding values calculated for NH_4VPO_4OH are listed for comparison.

To fall into the Haldane sector of the Sakai–Takahashi phase diagram, the system should satisfy the limiting value of $2J'/J < 0.0648$.[30] When $D/J > 0$, the Haldane phase persists up to the ratio $D/J = 1.033$.[31] Beyond this point, the quantum paramagnet phase appears. When $D/J < 0$, the Haldane phase persists down to the ratio $D/J = −0.316$,[32] below which the Néel phase appears. $(enH_2)_{0.5}VPO_4OH$ falls into the middle of Haldane sector of Sakai–Takahashi phase diagram, while NH_4VPO_4OH falls closer to the verge of this sector.[2]

Discussion

It is noted that the intrachain exchange J is stronger for $(enH_2)_{0.5}VPO_4OH$ than for NH_4VPO_4OH by a factor of about 1.6, while the interchain exchange J' is much weaker than the intrachain exchange J in both $(enH_2)_{0.5}VPO_4OH$ and NH_4VPO_4OH. These observations originate from the fact that each $V^{3+}\cdots V^{3+}$ chain along the b-axis is a consequence of the edge-sharing between adjacent $VO_5(OH)$ octahedra, with the shared edges forming a ribbon chain along the b-axis (Fig. 1b, S4 and S5†). It is convenient to distinguish two different kinds of O atoms in each ribbon chain; the O atoms involved in the edge-sharing will be referred to as the equatorial O atoms, O_{eq}, while the O atoms above and below each ribbon plane as the axial O atoms, O_{ax}. Each ribbon chain exhibits a slight twisting and zigzag bending in $(enH_2)_{0.5}VPO_4OH$, but it does not in NH_4VPO_4OH. If we take the local x-axis along the $V^{3+}\cdots V^{3+}$ direction (Fig. S6 of ESI†), and the xy plane parallel to the ribbon plane (disregarding the slight zigzag bending), then the t_{2g} set of each V^{3+} ion has the $x^2 − y^2$, xz and yz states. (If the local x-axis is chosen along a $V–O_{eq}$ bond, the t_{2g} set would be described by the xy, xz and yz states.) The direct $V^{3+}\cdots V^{3+}$ interaction is strong between the $x^2 − y^2$ states (Fig. 6a) and also between the xz states (Fig. 6b), so the t_{2g} set splits into the $(x^2 − y^2, xz)$ set lying below the yz state (Fig. 6c). This point was verified by calculating the partial density of states (PDOS) for $(enH_2)_{0.5}VPO_4OH$ and NH_4VPO_4OH (see the PDOS plots in Fig. S7 and S8 of ESI†). Thus, the $x^2 − y^2$ and xz states act as the magnetic orbitals of each V^{3+} ion. The $V^{3+}\cdots V^{3+}$ distance is slightly shorter for $(enH_2)_{0.5}VPO_4OH$ than for NH_4VPO_4OH[5] (3.058 $vs.$ 3.082 Å), so the direct $V^{3+}\cdots V^{3+}$ interaction is stronger and hence the intrachain exchange J becomes greater for $(enH_2)_{0.5}VPO_4OH$.

The reason why the interchain J' is very weak in $(enH_2)_{0.5}VPO_4OH$ and NH_4VPO_4OH is explained by analyzing how the two adjacent ribbon chains are interconnected by the PO_4 groups. As shown in Fig. 2b, the interchain spin exchange occurs through the $V–O\cdots P^{5+}\cdots O–V$ paths. Note that each PO_4 group corner-shares with one O_{eq} of one ribbon chain and with two O_{ax} atoms of the other ribbon chain such that the $V–O\cdots P^{5+}\cdots O–V$ paths are of the $V–O_{eq}\cdots P^{5+}\cdots O_{ax}–V$ type. (The fourth O atom of PO_4 makes hydrogen bonds with two different enH_2^{2+} cations, Fig. 2a.) The latter practically vanishes because the $x^2 − y^2$ and xz magnetic orbitals do not have their p-orbital tails on both $V–O_{eq}$ and $V–O_{ax}$ bonds (Fig. S9 of ESI†).

We now discuss why the V^{3+} ions in the ribbon chains of $(enH_2)_{0.5}VPO_4OH$ and NH_4VPO_4OH exhibit a very weak single-ion anisotropy. The d-states of the V^{3+} ion in each VO_6 octahedron in these magnets are split as shown in Fig. 6c. The preferred spin orientation of a magnetic ion is predicted by the selection rule[22,33] based on the interaction of the highest-occupied state with the lowest-unoccupied state, which is induced

Table 2 Values of J, J', D and $\Delta = 0.41 J$ values (in K) calculated for $(enH_2)_{0.5}VPO_4OH$ and NH_4VPO_4OH

Magnet	U_{eff}	J	J'	D	$2J'/J$	D/J	Δ
$(enH_2)_{0.5}VPO_4OH$	2	146.8	−0.38	0.23	$−5.2 \times 10^{-3}$	1.57×10^{-3}	60.2
	3	121.3	0.38	0.12	3.1×10^{-3}	9.89×10^{-4}	49.7
NH_4VPO_4OH	2	92.8	3.28	0.12	7.1×10^{-2}	1.29×10^{-3}	38.0
	3	73.0	3.02	0.12	3.3×10^{-2}	1.64×10^{-3}	29.9
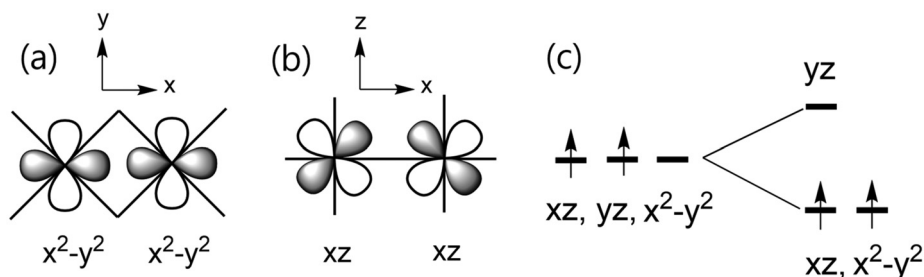
Fig. 6 (a) Direct $V^{3+}\cdots V^{3+}$ interaction between the $x^2 − y^2$ orbitals across the shared edge. (b) Direct $V^{3+}\cdots V^{3+}$ interaction between the xz orbitals across the shared edge. (c) Split of the t_{2g} set by the direct $V^{3+}\cdots V^{3+}$ interaction.

by spin–orbit coupling (SOC). This selection rule predicts that the interaction of the occupied xz state with the unoccupied yz state favours the spin orientation along the local c-axis, but that of the occupied $x^2 - y^2$ state with the unoccupied yz state favours the spin orientation perpendicular to the local c-axis. The presence of the two opposing trends leads to a very weak magnetic anisotropy.

Conclusion

To summarize, we observed a Haldane magnetic behaviour in the first V-based organically templated magnet $(enH_2)_{0.5}VPO_4OH$ from magnetic susceptibility and NMR measurements. The energy gap $\Delta = 59.3$ K between the spin-singlet ground state and the triplet excited states is observed from the $\chi(T)$ curve taken at $\mu_0H = 0.1$ T, and this gap is reduced to 48.4 K at $\mu_0H = 9$ T as observed from the ^{31}P shift. The NMR results indicate that the Haldane $S = 1$ spin chain segments are much longer in $(enH_2)_{0.5}VPO_4OH$ than in its ammonium counterpart NH_4VPO_4OH, and that a spin-glass ground state of unpaired $S = 1/2$ spins forms at $T_{S–G} \approx 3$ K as observed in NH_4VPO_4OH. The parameters J, J' and D describing this magnet were evaluated and compared with those in NH_4VPO_4OH. The reasons for the weaker interchain exchange interaction J' and single-ion anisotropy D compared to the intrachain exchange interaction J are two-fold: one is that the t_{2g} state of each V^{3+} ions split into the $(x^2 - y^2, xz)$ state below the yz state (with the x-axis taken along the $V^{3+}\cdots V^{3+}$ direction), and the other is that the PO_4 groups interconnecting adjacent ribbon chains lead to the $V–O_{eq}\cdots P^{5+}\cdots O_{ax}–V$ type spin exchanges.

Data availability

ESI,† including details on synthesis, crystal structure, nuclear magnetic resonance are theoretical DFT calculations for $(enH_2)_{0.5}VPO_4OH$, are available at **https://doi.org/DOI**. Crystallographic data for $(enH_2)_{0.5}VPO_4OH$ has been deposited at the CCDC under CCDC 2356612.

Conflicts of interest

There are no conflicts to declare.

Acknowledgements

References

1 F. D. M. Haldane, Continuum dynamics of the 1-D Heisenberg antiferromagnet: Identification with the O(3) nonlinear sigma model, *Phys. Lett. A*, 1983, **93**, 464; F. D. M. Haldane, Nonlinear Field Theory of Large-Spin Heisenberg Antiferromagnets: Semiclassically Quantized Solitons of the One-Dimensional Easy-Axis Néel State, *Phys. Rev. Lett.*, 1983, **50**, 1153.

2 T. Sakai and M. Takahashi, Effect of the Haldane gap on quasi-one-dimensional systems, *Phys. Rev. B: Condens. Matter Mater. Phys.*, 1990, **42**, 4537.

3 P. Tin, M. J. Jenkins, J. Xing, N. Caci, Z. Gai, R. Jin, S. Wessel, J. Krzystek, C. Li, L. L. Daemen, Y. Cheng and Z.-L. Xue, Haldane topological spin-1 chains in a planar metal-organic framework, *Nat. Commun.*, 2023, **14**, 5454.

4 O. V. Maximova, S. V. Streltsov and A. N. Vasiliev, Long range ordered, dimerized, large-D and Haldane phases in spin 1 chain compounds, *Crit. Rev. Solid State Mater. Sci.*, 2021, **46**, 371.

5 A. Sh. Samarin, I. A. Trussov, Z. V. Pchelkina, S. S. Fedotov, Y. A. Ovchenkov, S. V. Zhurenko, A. V. Tkachev, A. A. Gippius, L. V. Shvanskaya and A. N. Vasiliev, Lamellar crystal structure and Haldane magnetism in NH_4VPO_4OH, *ACIE*, 2023, **63**, e202316719.

6 A. A. Coelho, TOPAS and TOPAS-Academic: an optimization program integrating computer algebra and crystallographic objects written in C++, *J. Appl. Crystallogr.*, 2018, **51**, 210.

7 M. Cavellec, D. Riou and G. Ferey, A Two-dimensional iron phosphate templated by ethylenediamine, *Acta Crystallogr., Sect. C: Cryst. Struct. Commun.*, 1995, **51**, 2242.

8 R. H. Jones, J. M. Thomas, H. Qisheng, M. B. Hursthouse and J. Chen, The synthesis and crystal structure of a novel clay-like gallophosphate with sub-unit-cell intergrowths of ethylenediamine: $[GaPO_4(OH)]^-$ $0\cdot5(H_3NCH_2CH_2NH_3)^{2+}$, *J. Chem. Soc., Chem. Commun.*, 1991, 1520.

9 F. Bonhomme, S. G. Thoma and T. M. Nenoff, Two ammonium templated gallophosphates: synthesis and structure determination from powder diffraction data of 2D and 3D-GAPON, *Microporous Mesoporous Mater.*, 2002, **53**, 87.

10 F. P. Araujo, N. Hulsbosch and P. Muchez, High spatial resolution Raman mapping of complex mineral assemblages: Application on phosphate mineral sequences in pegmatites, *J. Raman Spectrosc.*, 2021, **52**, 690.

11 Y. Song, P. Y. Zavalij, N. A. Chernova, M. Suzuki and M. S. Whittingham, Comparison of one, two-, and three-

dimensional iron phosphates containing ethylenediamine, *J. Solid State Chem.*, 2003, **175**, 63.

12 L. Torre-Fernández, A. Espina, S. A. Khainakov, Z. Amghouz, J. R. García and S. García-Granda, Novel ethylenediamine-gallium phosphate containing 6-fold co-ordinated gallium atoms with unusual four equatorial Ga–N bonds, *J. Solid State Chem.*, 2014, **215**, 143.

13 A. John, D. Philip, K. Morgan and S. Devanarayanan, IR and Raman spectra of two layered aluminium phosphates $Co(en)_3Al_3P_4O_{16} \cdot 3H_2O$ and $[NH_4]_3[Co(NH_3)_6]_3[Al_2(PO_4)_4]_2 \cdot 2H_2O$, *Spectrochim. Acta, Part A*, 2000, **56**, 2715.

14 J. Escobal, J. L. Pizarro, J. L. Mesa, M. I. Arriortua and T. Rojo, An ionic nickel(II) phosphate with ethylenediamine: $(C_2H_{10}N_2)[Ni(H_2O)_6](HPO_4)_2$. Hydrothermal synthesis, crystal structure, and spectroscopic properties, *J. Solid State Chem.*, 2000, **154**, 460.

15 A. K. Bera, B. Lake, A. T. M. N. Islam, B. Klemke, E. Faulhaber and J. M. Law, Field-induced magnetic ordering and single-ion anisotropy in the quasi-one-dimensional Haldane chain compound $SrNi_2V_2O_8$: A single-crystal investigation, *Phys. Rev. B: Condens. Matter Mater. Phys.*, 2013, **87**, 224423.

16 G. A. Bain and J. F. Berry, Diamagnetic corrections and Pascal's constants, *J. Chem. Educ.*, 2008, **85**, 532.

17 A. P. Bussandri and M. J. Zuriaga, Spin-echo mapping spectroscopy applied to NQR, *J. Magn. Reson.*, 1998, **131**, 224.

18 W. G. Clark, M. E. Hanson, F. Lefloch and P. Ségransan, Magnetic resonance spectral reconstruction using frequency–shifted and summed Fourier transform processing, *Rev. Sci. Instrum.*, 1995, **66**, 2453.

19 Y. Y. Tong, Nuclear spin-echo Fourier-transform mapping spectroscopy for broad NMR lines in solids, *J. Magn. Reson., Ser. A*, 1996, **119**, 22.

20 S. Kundu, T. Dey, A. V. Mahajan and N. Büttgen, $LiZn_2V_3O_8$: a new geometrically frustrated cluster spin-glass, *J. Phys.: Condens. Matter*, 2020, **32**, 115601.

21 X. Zong, A. Niazi, F. Borsa, X. Ma and D. C. Johnston, Structure, magnetization, and NMR studies of the spin-glass compound $(Li_xV_{1-x})_3BO_5$ ($x \approx 0.40$ and 0.33), *Phys. Rev. B: Condens. Matter Mater. Phys.*, 2007, **76**, 054452.

22 H. Xiang, C. Lee, H.-J. Koo, X. Gong and M.-H. Whangbo, Magnetic properties and energy-mapping analysis, *Dalton Trans.*, 2013, **42**, 823.

23 M.-H. Whangbo and H. Xiang, *Magnetic Properties from the Perspectives of Electronic Hamiltonian, Handbook of Solid State Chemistry*, 2017.

24 M.-H. Whangbo, H.-J. Koo and R. K. Kremer, Spin exchanges between transition metal ions governed by the ligand p-orbitals in their magnetic orbitals, *Molecules*, 2021, **26**, 531.

25 G. Kresse and D. Joubert, From ultrasoft pseudopotentials to the projector augmented-wave method, *Phys. Rev. B: Condens. Matter Mater. Phys.*, 1999, **59**, 1758.

26 J. P. Perdew, K. Burke and M. Ernzerhof, Generalized gradient approximation made simple, *Phys. Rev. Lett.*, 1996, **77**, 3865.

27 G. Kresse and J. Furthmüller, Efficiency of ab-initio total energy calculations for metals and semiconductors using a plane-wave basis set, *Comput. Mater. Sci.*, 1996, **6**, 15.

28 S. L. Dudarev, G. A. Botton, S. Y. Savrasov, C. J. Humphreys and A. P. Sutton, Electron-energy-loss spectra and the structural stability of nickel oxide: An LSDA+U study, *Phys. Rev. B: Condens. Matter Mater. Phys.*, 1998, **57**, 1505.

29 J. Kuneš, P. Novák, R. Schmid, P. Blaha and K. Schwarz, Electronic structure of fcc Th: Spin-orbit calculation with $6p_{1/2}$ local orbital extension, *Phys. Rev. B: Condens. Matter Mater. Phys.*, 2001, **64**, 153102.

30 K. Wierschem and P. Sengupta, Characterizing the Haldane phase in quasi-one-dimensional spin-1 Heisenberg antiferromagnets, *Mod. Phys. Lett. B*, 2014, **28**, 1430017.

31 K. Wierschem and P. Sengupta, Quenching the Haldane gap in spin-1 Heisenberg antiferromagnets, *Phys. Rev. Lett.*, 2014, **112**, 247203.

32 W. J. Rao, G. Y. Zhu and G. M. Zhang, SU(3) quantum critical model emerging from a spin-1 topological phase, *Phys. Rev. B*, 2016, **93**, 165135.

33 M.-H. Whangbo, E. E. Gordon, H. J. Xiang, H.-J. Koo and C. Lee, Prediction of spin orientations in terms of HOMO–LUMO interactions using spin-orbit coupling as perturbation, *Acc. Chem. Res.*, 2015, **48**, 3080.